

**Measurement of the Cross-Section for
the Process $\gamma\gamma \rightarrow p\bar{p}$ at
 $\sqrt{s_{ee}} = 183 - 189 \text{ GeV}$ at LEP**

The OPAL Collaboration

Abstract

The exclusive production of proton-antiproton pairs in the collisions of two quasi-real photons has been studied using data taken at $\sqrt{s_{ee}} = 183 \text{ GeV}$ and 189 GeV with the OPAL detector at LEP. Results are presented for $p\bar{p}$ invariant masses, W , in the range $2.15 < W < 3.95 \text{ GeV}$. The cross-section measurements are compared with previous data and with recent analytic calculations based on the quark-diquark model.

(To be submitted to Eur. Phys. J. C.)

The OPAL Collaboration

G. Abbiendi², C. Ainsley⁵, P.F. Åkesson³, G. Alexander²², J. Allison¹⁶, P. Amaral⁹,
G. Anagnostou¹, K.J. Anderson⁹, S. Arcelli², S. Asai²³, D. Axen²⁷, G. Azuelos^{18,a}, I. Bailey²⁶,
E. Barberio⁸, T. Barillari², R.J. Barlow¹⁶, R.J. Batley⁵, P. Bechtel²⁵, T. Behnke²⁵, K.W. Bell²⁰,
P.J. Bell¹, G. Bella²², A. Bellerive⁶, G. Benelli⁴, S. Bethke³², O. Biebel³¹, I.J. Bloodworth¹,
O. Boeriu¹⁰, P. Bock¹¹, D. Bonacorsi², M. Boutemeur³¹, S. Braibant⁸, L. Brigliadori²,
R.M. Brown²⁰, K. Buesser²⁵, H.J. Burckhart⁸, S. Campana⁴, R.K. Carnegie⁶, B. Caron²⁸,
A.A. Carter¹³, J.R. Carter⁵, C.Y. Chang¹⁷, D.G. Charlton^{1,b}, A. Csilling^{8,g}, M. Cuffiani²,
S. Dado²¹, G.M. Dallavalle², S. Dallison¹⁶, A. De Roeck⁸, E.A. De Wolf⁸, K. Desch²⁵,
B. Dienes³⁰, M. Donkers⁶, J. Dubbert³¹, E. Duchovni²⁴, G. Duckeck³¹, I.P. Duerdoth¹⁶,
E. Elfgrén¹⁸, E. Etzion²², F. Fabbri², L. Feld¹⁰, P. Ferrari⁸, F. Fiedler³¹, I. Fleck¹⁰, M. Ford⁵,
A. Frey⁸, A. Fürtjes⁸, P. Gagnon¹², J.W. Gary⁴, G. Gaycken²⁵, C. Geich-Gimbel³,
G. Giacomelli², P. Giacomelli², M. Giunta⁴, J. Goldberg²¹, E. Gross²⁴, J. Grunhaus²²,
M. Gruwé⁸, P.O. Günther³, A. Gupta⁹, C. Hajdu²⁹, M. Hamann²⁵, G.G. Hanson⁴, K. Harder²⁵,
A. Harel²¹, M. Harin-Dirac⁴, M. Hauschild⁸, J. Hauschildt²⁵, C.M. Hawkes¹, R. Hawkings⁸,
R.J. Hemingway⁶, C. Hensel²⁵, G. Herten¹⁰, R.D. Heuer²⁵, J.C. Hill⁵, K. Hoffman⁹,
R.J. Homer¹, D. Horváth^{29,c}, R. Howard²⁷, P. Hüntemeyer²⁵, P. Igo-Kemenes¹¹, K. Ishii²³,
H. Jeremie¹⁸, P. Jovanovic¹, T.R. Junk⁶, N. Kanaya²⁶, J. Kanzaki²³, G. Karapetian¹⁸,
D. Karlen⁶, V. Kartvelishvili¹⁶, K. Kawagoe²³, T. Kawamoto²³, R.K. Keeler²⁶, R.G. Kellogg¹⁷,
B.W. Kennedy²⁰, D.H. Kim¹⁹, K. Klein¹¹, A. Klier²⁴, S. Kluth³², T. Kobayashi²³, M. Kobel³,
S. Komamiya²³, L. Kormos²⁶, R.V. Kowalewski²⁶, T. Krämer²⁵, T. Kress⁴, P. Krieger^{6,l}, J. von
Krogh¹¹, D. Krop¹², K. Kruger⁸, M. Kupper²⁴, G.D. Lafferty¹⁶, H. Landsman²¹, D. Lanske¹⁴,
J.G. Layter⁴, A. Leins³¹, D. Lellouch²⁴, J. Letts¹², L. Levinson²⁴, J. Lillich¹⁰, S.L. Lloyd¹³,
F.K. Loebinger¹⁶, J. Lu²⁷, J. Ludwig¹⁰, A. Macpherson^{28,i}, W. Mader³, S. Marcellini²,
T.E. Marchant¹⁶, A.J. Martin¹³, J.P. Martin¹⁸, G. Masetti², T. Mashimo²³, P. Mättig^m,
W.J. McDonald²⁸, J. McKenna²⁷, T.J. McMahon¹, R.A. McPherson²⁶, F. Meijers⁸,
P. Mendez-Lorenzo³¹, W. Menges²⁵, F.S. Merritt⁹, H. Mes^{6,a}, A. Michelini², S. Mihara²³,
G. Mikenberg²⁴, D.J. Miller¹⁵, S. Moed²¹, W. Mohr¹⁰, T. Mori²³, A. Mutter¹⁰, K. Nagai¹³,
I. Nakamura²³, H.A. Neal³³, R. Nisius⁸, S.W. O’Neale¹, A. Oh⁸, A. Okpara¹¹, M.J. Oreglia⁹,
S. Orito²³, C. Pahl³², G. Pásztor^{4,g}, J.R. Pater¹⁶, G.N. Patrick²⁰, J.E. Pilcher⁹, J. Pinfold²⁸,
D.E. Plane⁸, B. Poli², J. Polok⁸, O. Pooth¹⁴, M. Przybycień^{8,n}, A. Quadt³, K. Rabbertz⁸,
C. Rembser⁸, P. Renkel²⁴, H. Rick⁴, J.M. Roney²⁶, S. Rosati³, Y. Rozen²¹, K. Runge¹⁰,
K. Sachs⁶, T. Saeki²³, O. Sahr³¹, E.K.G. Sarkisyan^{8,j}, A.D. Schaile³¹, O. Schaile³¹,
P. Scharff-Hansen⁸, J. Schieck³², T. Schoerner-Sadenius⁸, M. Schröder⁸, M. Schumacher³,
C. Schwick⁸, W.G. Scott²⁰, R. Seuster^{14,f}, T.G. Shears^{8,h}, B.C. Shen⁴,
C.H. Shepherd-Themistocleous⁵, P. Sherwood¹⁵, G. Siroli², A. Skuja¹⁷, A.M. Smith⁸, R. Sobie²⁶,
S. Söldner-Rembold^{10,d}, S. Spagnolo²⁰, F. Spano⁹, A. Stahl³, K. Stephens¹⁶, D. Strom¹⁹,
R. Ströhmer³¹, S. Tarem²¹, M. Tasevsky⁸, R.J. Taylor¹⁵, R. Teuscher⁹, M.A. Thomson⁵,
E. Torrence¹⁹, D. Toya²³, P. Tran⁴, T. Trefzger³¹, A. Tricoli², I. Trigger⁸, Z. Trócsányi^{30,e},
E. Tsur²², M.F. Turner-Watson¹, I. Ueda²³, B. Ujvári^{30,e}, B. Vachon²⁶, C.F. Vollmer³¹,
P. Vannerem¹⁰, M. Verzocchi¹⁷, H. Voss⁸, J. Vossebeld^{8,h}, D. Waller⁶, C.P. Ward⁵, D.R. Ward⁵,
P.M. Watkins¹, A.T. Watson¹, N.K. Watson¹, P.S. Wells⁸, T. Wengler⁸, N. Wormes³,
D. Wetterling¹¹, G.W. Wilson^{16,k}, J.A. Wilson¹, G. Wolf²⁴, T.R. Wyatt¹⁶, S. Yamashita²³,
D. Zer-Zion⁴, L. Zivkovic²⁴

- ¹School of Physics and Astronomy, University of Birmingham, Birmingham B15 2TT, UK
- ²Dipartimento di Fisica dell' Università di Bologna and INFN, I-40126 Bologna, Italy
- ³Physikalisches Institut, Universität Bonn, D-53115 Bonn, Germany
- ⁴Department of Physics, University of California, Riverside CA 92521, USA
- ⁵Cavendish Laboratory, Cambridge CB3 0HE, UK
- ⁶Ottawa-Carleton Institute for Physics, Department of Physics, Carleton University, Ottawa, Ontario K1S 5B6, Canada
- ⁸CERN, European Organisation for Nuclear Research, CH-1211 Geneva 23, Switzerland
- ⁹Enrico Fermi Institute and Department of Physics, University of Chicago, Chicago IL 60637, USA
- ¹⁰Fakultät für Physik, Albert-Ludwigs-Universität Freiburg, D-79104 Freiburg, Germany
- ¹¹Physikalisches Institut, Universität Heidelberg, D-69120 Heidelberg, Germany
- ¹²Indiana University, Department of Physics, Swain Hall West 117, Bloomington IN 47405, USA
- ¹³Queen Mary and Westfield College, University of London, London E1 4NS, UK
- ¹⁴Technische Hochschule Aachen, III Physikalisches Institut, Sommerfeldstrasse 26-28, D-52056 Aachen, Germany
- ¹⁵University College London, London WC1E 6BT, UK
- ¹⁶Department of Physics, Schuster Laboratory, The University, Manchester M13 9PL, UK
- ¹⁷Department of Physics, University of Maryland, College Park, MD 20742, USA
- ¹⁸Laboratoire de Physique Nucléaire, Université de Montréal, Montréal, Quebec H3C 3J7, Canada
- ¹⁹University of Oregon, Department of Physics, Eugene OR 97403, USA
- ²⁰CLRC Rutherford Appleton Laboratory, Chilton, Didcot, Oxfordshire OX11 0QX, UK
- ²¹Department of Physics, Technion-Israel Institute of Technology, Haifa 32000, Israel
- ²²Department of Physics and Astronomy, Tel Aviv University, Tel Aviv 69978, Israel
- ²³International Centre for Elementary Particle Physics and Department of Physics, University of Tokyo, Tokyo 113-0033, and Kobe University, Kobe 657-8501, Japan
- ²⁴Particle Physics Department, Weizmann Institute of Science, Rehovot 76100, Israel
- ²⁵Universität Hamburg/DESY, Institut für Experimentalphysik, Notkestrasse 85, D-22607 Hamburg, Germany
- ²⁶University of Victoria, Department of Physics, P O Box 3055, Victoria BC V8W 3P6, Canada
- ²⁷University of British Columbia, Department of Physics, Vancouver BC V6T 1Z1, Canada
- ²⁸University of Alberta, Department of Physics, Edmonton AB T6G 2J1, Canada
- ²⁹Research Institute for Particle and Nuclear Physics, H-1525 Budapest, P O Box 49, Hungary
- ³⁰Institute of Nuclear Research, H-4001 Debrecen, P O Box 51, Hungary
- ³¹Ludwig-Maximilians-Universität München, Sektion Physik, Am Coulombwall 1, D-85748 Garching, Germany
- ³²Max-Planck-Institut für Physik, Föhringer Ring 6, D-80805 München, Germany
- ³³Yale University, Department of Physics, New Haven, CT 06520, USA

^a and at TRIUMF, Vancouver, Canada V6T 2A3

^b and Royal Society University Research Fellow

^c and Institute of Nuclear Research, Debrecen, Hungary

^d and Heisenberg Fellow

^e and Department of Experimental Physics, Lajos Kossuth University, Debrecen, Hungary

^f and MPI München

^g and Research Institute for Particle and Nuclear Physics, Budapest, Hungary

^h now at University of Liverpool, Dept of Physics, Liverpool L69 3BX, UK

ⁱ and CERN, EP Div, 1211 Geneva 23

^j and Universitaire Instelling Antwerpen, Physics Department, B-2610 Antwerpen, Belgium

^k now at University of Kansas, Dept of Physics and Astronomy, Lawrence, KS 66045, USA

^l now at University of Toronto, Dept of Physics, Toronto, Canada

^m current address Bergische Universität, Wuppertal, Germany

ⁿ and University of Mining and Metallurgy, Cracow, Poland

1 Introduction

The exclusive production of proton-antiproton ($p\bar{p}$) pairs in the collision of two quasi-real photons can be used to test predictions of QCD. At LEP the photons are emitted by the beam electrons¹ and the $p\bar{p}$ pairs are produced in the process $e^+e^- \rightarrow e^+e^-\gamma\gamma \rightarrow e^+e^-p\bar{p}$.

The application of QCD to exclusive photon-photon reactions is based on the work of Brodsky and Lepage [1]. According to their formalism the process is factorized into a non-perturbative part, which is the hadronic wave function of the final state, and a perturbative part. Calculations based on this ansatz [2, 3] use a specific model of the proton's three-quark wave function by Chernyak and Zhitnitsky [4]. This calculation yields cross-sections about one order of magnitude smaller than the existing experimental results [5–10], for $p\bar{p}$ centre-of-mass energies W greater than 2.5 GeV.

To model non-perturbative effects, the introduction of quark-diquark systems has been proposed [11]. Within this model, baryons are viewed as a combination of a quark and a diquark rather than a three-quark system. The composite nature of the diquark is taken into account by form factors.

Recent studies [12] have extended the systematic investigation of hard exclusive reactions within the quark-diquark model to photon-photon processes [13–16]. In these studies the cross-sections have been calculated down to W values of 2.2 GeV below which the quark-diquark model is no longer expected to be valid. Most of the experimental data, however, have been taken at such low energies.

The calculations of the integrated cross-section for the process $\gamma\gamma \rightarrow p\bar{p}$ in the angular range $|\cos\theta^*| < 0.6$ (where θ^* is the angle between the proton's momentum and the electron beam direction in the $p\bar{p}$ centre-of-mass system) and for $W > 2.5$ GeV are in good agreement with experimental results [9, 10], whereas the pure quark model predicts much smaller cross-sections [2, 3].

In this paper, we present a measurement of the cross-section for the exclusive process $e^+e^- \rightarrow e^+e^-p\bar{p}$ in the range $2.15 < W < 3.95$ GeV, using data taken with the OPAL detector at $\sqrt{s_{ee}} = 183$ GeV and 189 GeV at LEP. The integrated luminosities for the two energies are 62.8 pb^{-1} and 186.2 pb^{-1} .

¹In this paper positrons are also referred to as electrons.

2 The OPAL detector

The OPAL detector and trigger system are described in detail elsewhere [17]. We briefly describe only those features particularly relevant to this analysis. The tracking system for charged particles is inside a solenoid that provides a uniform axial magnetic field of 0.435 T. The system consists of a silicon micro-vertex detector, a high-resolution vertex drift chamber, a large-volume jet chamber and surrounding z -chambers. The micro-vertex detector surrounds the beam pipe covering the angular range of $|\cos\theta| < 0.9$ and provides tracking information in the r - ϕ and z directions². The jet chamber records the momentum and energy loss of charged particles over 98% of the solid angle. In the range of $|\cos\theta| < 0.73$, up to 159 points are measured along each track. The energy loss, dE/dx , of a charged particle in the chamber gas is measured from the integrated charges of each hit at both ends of each signal wire with a resolution of about 3.5% for isolated tracks with the maximum of 159 points. The z -chambers are used to improve the track measurement in the z direction.

The barrel time-of-flight (TOF) scintillation counters are located immediately outside the solenoid at a mean radius of 2.36 m, covering the polar angle range $|\cos\theta| < 0.82$. The outer parts of the detector, in the barrel and endcaps, consist of lead-glass electromagnetic calorimetry (ECAL) followed by an instrumented iron yoke for hadron calorimetry and four layers of external muon chambers. Forward electromagnetic calorimeters complete the acceptance for electromagnetically interacting particles down to polar angles of about 24 mrad.

The trigger signatures required for this analysis are based on a combination of time-of-flight and track trigger information.

3 Kinematics

The production of proton-antiproton pairs in photon-photon interactions proceeds via the process

$$e^+(p_1) + e^-(p_2) \rightarrow e^+(p'_1) + e^-(p'_2) + \gamma(q_1) + \gamma(q_2) \rightarrow e^+(p'_1) + e^-(p'_2) + p(q'_1) + \bar{p}(q'_2) \quad (1)$$

where q_i, p_i denote the four-momenta ($i = 1, 2$). Each of the two incoming electrons emits a photon and the final state produced by the two colliding photons consists of one proton (p) and one antiproton (\bar{p}). The four-momentum squared of the two photons is ($i = 1, 2$)

$$q_i^2 = -Q_i^2 = (p_i - p'_i)^2. \quad (2)$$

Since the electrons are scattered at small angles and they remain undetected, the four-momenta squared of each of the two photons are small, i.e. the photons are quasi-real. In this case the transverse³ component of the momentum sum of the proton and the antiproton in the laboratory system is expected to be small whereas the longitudinal component of the momentum sum can

²In the OPAL right-handed coordinate system the z -axis points along the e^- beam direction, and the x -axis points towards the centre of the LEP ring. The polar angle θ is defined with respect to the z -axis, and the azimuthal angle ϕ with respect to the x -axis.

³In this paper transverse momenta are always defined with respect to the z axis.

be large. The photon-photon centre-of-mass system is generally boosted along the beam axis. The larger the boost, the closer the produced (anti) protons are to the beam direction. This feature, combined with the typically low mass of the final state $p\bar{p}$, and the low efficiency for tracking at small angles, leads to significant acceptance losses for these types of events.

4 Monte Carlo generators

The $e^+e^- \rightarrow e^+e^-p\bar{p}$ events are simulated with the PC Monte Carlo generator which has been developed to study exclusive photon-photon processes [18]. The PC Monte Carlo generator has been expanded for use in this analysis to simulate the kinematics of exclusive baryon-antibaryon final states, $e^+e^- \rightarrow e^+e^-p\bar{p}$, $e^+e^- \rightarrow e^+e^-\Lambda\bar{\Lambda}$, and $e^+e^- \rightarrow e^+e^-\Xi^-\Xi^+$. A total of 20 000 $e^+e^- \rightarrow e^+e^-p\bar{p}$ Monte Carlo events have been generated as a control sample for the event selection described in the next section. Similarly, for the trigger and detection efficiency determination, a total of 360 000 $e^+e^- \rightarrow e^+e^-p\bar{p}$ Monte Carlo events have been generated in the range of $2.15 < W < 3.95$ GeV. The background coming from $e^+e^- \rightarrow e^+e^-\pi^+\pi^-$ is generated with the PC Monte Carlo program, as is the feed-down background from proton-antiproton pairs coming from the reaction $e^+e^- \rightarrow e^+e^-\Lambda\bar{\Lambda} \rightarrow p\bar{p}\pi^+\pi^-$ where the pions are not detected (200 000 events).

The leptonic photon-photon background processes $e^+e^- \rightarrow e^+e^-\mu^+\mu^-$, $e^+e^- \rightarrow e^+e^-e^+e^-$ and $e^+e^- \rightarrow e^+e^-\tau^+\tau^-$ are simulated with the Vermaseren generator [19]. The KORALZ generator [20] is used to simulate the background processes $e^+e^- \rightarrow \mu^+\mu^-$, and $e^+e^- \rightarrow \tau^+\tau^-$. The $e^+e^- \rightarrow e^+e^-$ background process is simulated with the BHWIDE [21] generator. Table 1 lists all the generated background Monte Carlo samples.

Monte Carlo events are generated at $\sqrt{s_{ee}} = 189$ GeV only, since the change in acceptance between $\sqrt{s_{ee}} = 183$ and 189 GeV is small compared to the statistical uncertainty of the measurement. They have been processed through a full simulation of the OPAL detector [22] and have been analysed using the same reconstruction algorithms that are used for the data.

5 Event selection

The $e^+e^- \rightarrow e^+e^-p\bar{p}$ events are selected by the following set of cuts:

1. The sum of the energies measured in the barrel and endcap sections of the electromagnetic calorimeter must be less than half the beam energy.
2. Exactly two oppositely charged tracks are required with each track having at least 20 hits in the central jet chamber to ensure a reliable determination of the specific energy loss dE/dx . The point of closest approach to the interaction point must be less than 1 cm in the $r\phi$ plane and less than 50 cm in the z direction.

3. For each track the polar angle must be in the range $|\cos\theta| < 0.75$ and the transverse momentum p_{\perp} must be larger than 0.4 GeV. These cuts ensure a high trigger efficiency and good particle identification.
4. The invariant mass W of the $p\bar{p}$ final state must be in the range $2.15 < W < 3.95$ GeV. The invariant mass is determined from the measured momenta of the two tracks using the proton mass.
5. The events are boosted into the rest system of the measured $p\bar{p}$ final state. The scattering angle of the tracks in this system has to satisfy $|\cos\theta^*| < 0.6$.
6. All events must fulfil the trigger conditions defined in Section 6.
7. The large background from other exclusive processes, mainly the production of e^+e^- , $\mu^+\mu^-$, and $\pi^+\pi^-$ pairs, is reduced by particle identification using the specific energy loss dE/dx in the jet chamber and the energy in the electromagnetic calorimeter. The dE/dx probabilities of the tracks must be consistent with the p and \bar{p} hypothesis.
 - Events where the ratio E/p for each track lies in the range $0.4 < E/p < 1.8$ ⁴ are regarded as possible $e^+e^- \rightarrow e^+e^-e^+e^-$ candidates. These events are rejected if the dE/dx probabilities of the two tracks are consistent with the electron hypothesis.
 - Events where the ratio E/p for each track is less than 0.8, as expected for a minimum ionizing particle, are regarded as possible background from $e^+e^- \rightarrow e^+e^-\mu^+\mu^-$ events. This background is reduced by rejecting events where the dE/dx probability for both tracks is consistent with the muon hypothesis. This cut is also effective in reducing the $\pi^+\pi^-$ background.
 - The dE/dx probability for the proton hypothesis has to be greater than 0.1% for each track and it has to be larger than the probabilities for the pion and kaon hypotheses. The product of the dE/dx probabilities for both tracks to be (anti) protons has to be larger than the product of the dE/dx probabilities for both tracks to be electrons.
8. Cosmic ray background is eliminated by applying a muon veto [23].
9. Exclusive two-particle final states are selected by requiring the transverse component of the momentum sum squared of the two tracks, $|\sum \vec{p}_{\perp}|^2$, to be smaller than 0.04 GeV². By restricting the maximum value of Q_i^2 , this cut also ensures that the interacting photons are quasi-real. Therefore no further cut rejecting events with scattered electrons in the detector needs to be applied. Fig. 1 shows the $|\sum \vec{p}_{\perp}|^2$ distribution obtained after applying all cuts except the cut on $|\sum \vec{p}_{\perp}|^2$.

After all cuts 163 data events are selected, 35 events at $\sqrt{s_{ee}} = 183$ GeV and 128 events at $\sqrt{s_{ee}} = 189$ GeV. The distribution of measured dE/dx values versus the particle momentum for the selected data events is shown in Fig. 2a. Background from events containing particles other than (anti-)protons is negligible due to the good rejection power of the dE/dx cuts. Since no event remains after applying the event selection to the background Monte Carlo samples, the 95% confidence level upper limits for the number of background events expected to contribute to the selected data sample are given in Table 1.

⁴ E here is the energy of the ECAL cluster associated with the track with momentum p .

Since the $p\bar{p}$ final state is fully reconstructed, the experimental resolution for W (determined with Monte Carlo simulation) is better than 1%. The experimental resolution for $|\cos\theta^*|$ is about 0.014. Fig. 2b shows the W distribution for data and Monte Carlo signal events after the final selection. The Monte Carlo distributions agree well with the data.

6 Trigger and detection efficiencies

The $e^+e^- \rightarrow e^+e^-p\bar{p}$ events contain only two tracks with momenta in the range 0.4 GeV to 2 GeV. Special triggers are required to select such low multiplicity events with only low momentum particles and the efficiencies of these triggers must be well known. The $e^+e^- \rightarrow e^+e^-p\bar{p}$ events are mainly triggered by a combination of triggers using hits in the time-of-flight counters and tracks. The track trigger takes data on the z coordinate of hits from the vertex drift chamber, and from three groups of 12 wires in the jet chamber. The selected events must satisfy at least one of the following trigger conditions:

- A Two tracks in the barrel region from the track-trigger (TT). This corresponds to an angular acceptance of approximately $|\cos\theta| < 0.75$.
- B A coincidence of at least one barrel track from the track trigger and a $\theta - \phi$ coincidence of a track from the track trigger with hits from the time-of-flight detector (TOF). The barrel track and the track forming the $\theta - \phi$ coincidence are not necessarily identical. The angular acceptance of the track trigger is approximately $|\cos\theta| < 0.75$, whereas the acceptance of the $\theta - \phi$ coincidence is $|\cos\theta| < 0.82$.

Condition A is highly efficient for events within its geometrical acceptance but it triggers on two tracks. Condition B is used to trigger on a single track and to measure the trigger efficiency in combination with condition A.

It was checked that the trigger efficiency does not depend on ϕ . Under this condition and assuming the efficiency of each trigger component for each track to be independent, the combined event trigger can be written as:

$$\varepsilon_{\text{TRIG}} = \varepsilon_{\text{TT}}^2 + 2\varepsilon_{\text{TT-TOF}}\varepsilon_{\text{TT}}(1 - \varepsilon_{\text{TT}}). \quad (3)$$

Here ε_{TT} is the efficiency for one track to be triggered by the track trigger and $\varepsilon_{\text{TT-TOF}}$ is the efficiency for one track to be triggered by the TT-TOF coincidence. The first term in (3) gives the efficiency for both tracks to be triggered by the track trigger (condition A) and the second term gives the efficiency for the events not triggered by condition A to be triggered by condition B for either of the two tracks.

Data events are used to calculate the trigger efficiency. The trigger efficiency is determined by considering events in which one track detected in one half of the $r\phi$ plane (e.g. $0 < \phi < 180$ degrees) satisfies the required track trigger and time-of-flight $\theta - \phi$ matching hit while the other track in the other half plane (e.g. $180 < \phi < 360$ degrees) is used to measure the efficiency of the track and time-of-flight triggers.

The efficiencies measured from the 163 selected events are $\varepsilon_{\text{TT}} = (93.7 \pm 1.7)\%$ and $\varepsilon_{\text{TT-TOF}} = (58.5 \pm 2.3)\%$, where the uncertainties are statistical only. This yields an overall event trigger efficiency of $\varepsilon_{\text{TRIG}} = (94.7 \pm 1.5)\%$, determined from data only.

To study the efficiency with a large event sample, events from photon-photon processes with two tracks in the final state such as e^+e^- and $\mu^+\mu^-$ are used together with the $p\bar{p}$ events to determine the track trigger efficiency as a function of p_\perp . This efficiency exceeds 90% for $p_\perp > 0.4$ GeV and the observed dependence of the track trigger efficiency on p_\perp is found to be consistent between electrons and muons.

In a second step, $e^+e^- \rightarrow e^+e^-p\bar{p}$ Monte Carlo events in the range $2.15 < W < 3.95$ GeV are used to obtain the trigger efficiencies as a function of W , $\varepsilon_{\text{TRIG}}(W)$. The Monte Carlo events are reweighted here according to the trigger efficiency which has been determined as a function of the transverse momentum p_\perp using (3). These reweighted Monte Carlo events have been used only to determine the trigger efficiency as function of W . Finally the values obtained for $\varepsilon_{\text{TRIG}}(W)$ are normalized to give the overall trigger efficiency $\varepsilon_{\text{TRIG}} = 94.7\%$ above the threshold $p_\perp > 0.4$ GeV as already determined from data only. The region $W < 2.15$ GeV is excluded from the analysis because the trigger efficiency drops rapidly below 70%.

The detection efficiency is determined by comparing the number of Monte Carlo events passing all cuts with the total number of Monte Carlo events generated within a polar angle $|\cos \theta_{\text{GEN}}^*| < 0.6$ in the $p\bar{p}$ centre-of-mass system:

$$\varepsilon_{\text{DET}} = \frac{d\sigma/dW(|\cos \theta^*|)}{d\sigma/dW(|\cos \theta_{\text{GEN}}^*|)}, \quad (4)$$

where $|\cos \theta^*|$ refers to the reconstructed polar angle in the $p\bar{p}$ centre-of-mass system. The detection efficiency is about 2% at high W and about 4% at low W . To be able to compare the measured cross-section with any given model in bins of $|\cos \theta^*|$ and W , the detection efficiency has been determined from the signal Monte Carlo in bins of W and $|\cos \theta^*|$.

7 Cross-section measurements

The differential cross-section for the process $e^+e^- \rightarrow e^+e^-p\bar{p}$ is given by

$$\frac{d^2\sigma(e^+e^- \rightarrow e^+e^-p\bar{p})}{dW d|\cos \theta^*|} = \frac{N_{\text{ev}}(W, |\cos \theta^*|)}{\mathcal{L}_{e^+e^-} \varepsilon_{\text{TRIG}} \varepsilon_{\text{DET}}(W, |\cos \theta^*|) \Delta W \Delta|\cos \theta^*|} \quad (5)$$

where N_{ev} is the number of events selected in each $(W, |\cos \theta^*|)$ bin, $\varepsilon_{\text{TRIG}}$ is the trigger efficiency, ε_{DET} is the detection efficiency, $\mathcal{L}_{e^+e^-}$ is the measured integrated luminosity, and ΔW and $\Delta|\cos \theta^*|$ are the bin widths in W and in $|\cos \theta^*|$.

The total cross-section $\sigma(\gamma\gamma \rightarrow p\bar{p})$ for a given value of $\sqrt{s_{\text{ee}}}$ is obtained from the differential cross-section $d\sigma(e^+e^- \rightarrow e^+e^-p\bar{p})/dW$ using the luminosity function $d\mathcal{L}_{\gamma\gamma}/dW$ [24]:

$$\sigma(\gamma\gamma \rightarrow p\bar{p}) = \frac{d\sigma(e^+e^- \rightarrow e^+e^-p\bar{p})}{dW} \bigg/ \frac{d\mathcal{L}_{\gamma\gamma}}{dW}. \quad (6)$$

The luminosity function $d\mathcal{L}_{\gamma\gamma}/dW$ is calculated by the GALUGA program [25]. The resulting differential cross-sections for the process $\gamma\gamma \rightarrow p\bar{p}$ in bins of W and $|\cos\theta^*|$ are then summed over $|\cos\theta^*|$ to obtain the total cross-section as a function of W for $|\cos\theta^*| < 0.6$.

8 Systematic uncertainties

The following sources of systematic uncertainties have been taken into account (Table 5):

Luminosity function: The accuracy of the photon-photon luminosity function used in (6) has been estimated by taking into account different models such as the ρ -pole model [26], the Equivalent Photon Approximation (EPA) [27], the Generalized Vector Dominance Model (GVMD) [25], the luminosity functions given in [28], and in [29, 30]. Each of the resulting numbers has then been compared with the VDM form-factor model [25] which is used for the final result. We take the largest deviation resulting from these comparisons as the uncertainty in the luminosity functions which is about $\pm 5\%$.

Trigger efficiency: The trigger efficiency model of (3) has been tested by making a comparison between the measured relative frequencies of the four different sub-combinations, $(N_{\text{TT}}, N_{\text{TT-TOF}}) = (1,1), (2,0), (2,1), (2,2)$, which can trigger the events, and the predicted values, by using fitted efficiencies for TT and TT-TOF (Section 6). Here N_{TT} denotes the number of tracks triggered by the TT and $N_{\text{TT-TOF}}$ the number of tracks triggered by the TT-TOF trigger. Table 2 gives the measured and predicted fractions for events with $W > 2.15$ GeV. The fit of the two efficiencies ε_{TT} and $\varepsilon_{\text{TT-TOF}}$ yields a χ^2 of 9.6 over 2 degrees of freedom. Although the fit is poor the overall efficiency result is consistent with the other determination. An additional systematic uncertainty of 5.0% is therefore assigned to the trigger efficiency. This value is obtained by increasing the uncertainties to obtain a normalized χ^2 of one.

Monte Carlo statistics: The statistical uncertainty on the detection efficiency due to the number of simulated Monte Carlo events varies from 4.5% at low W to 6% at high W .

dE/dx cuts: The systematic uncertainties due to the dE/dx cuts are determined by recalculating the Monte Carlo detection efficiency after varying the dE/dx values:

- The measured values are shifted by $\pm 1\sigma$, where σ is the theoretical uncertainty of the measurement.
- The measured values are smeared with a Gaussian distribution of width 0.1σ , which is the typical systematic uncertainty of each individual dE/dx measurement, as found for pions from K^0 decays [31].

The modified dE/dx values are transformed into weights and the new detection efficiency is calculated by applying the event selection on the modified Monte Carlo events. The systematic uncertainty assigned to each $(W, |\cos\theta^*|)$ bin is the quadratic sum of the full deviation of the detection efficiency with smearing and the average absolute deviation value of the $\pm 1\sigma$ shifted values with respect to the original values.

The systematic uncertainties due to the variation of the dE/dx cuts are larger at high values of W . They vary between 0.1% for $W < 2.6$ GeV and up to 5% for $W > 2.6$ GeV.

Residual background: Residual background can come from non-exclusive production of $p\bar{p}$ pairs in processes like $e^+e^- \rightarrow e^+e^-p\bar{p}\pi\pi$ if the pions are not detected. The $|\sum \vec{p}_\perp|^2$ cut eliminates most of this background. The data events are almost coplanar, i.e. no data event has an acoplanarity of more than 0.262 rad. To estimate the contribution of this background, the shape of the acoplanarity distribution for $p\bar{p}$ pairs in Monte Carlo $e^+e^- \rightarrow e^+e^-\Lambda\bar{\Lambda}$ and $e^+e^- \rightarrow e^+e^-p\bar{p}$ events has been fitted to the data. This yields an upper limit of 10 events for this background contribution. An additional systematic uncertainty of 6% is therefore taken into account.

Additional uncertainties due to the measured integrated e^+e^- luminosity, the track reconstruction efficiency and the momentum resolution for the protons are negligible. The total systematic uncertainty is obtained by adding all systematic uncertainties in quadrature.

9 Results and Discussion

The measured cross-sections in bins of W are given in Table 3. The average $\langle W \rangle$ in each bin has been determined by applying the procedure described in [32]. The measured cross-sections $\sigma(\gamma\gamma \rightarrow p\bar{p})$ for $2.15 < W < 3.95$ GeV and for $|\cos\theta^*| < 0.6$ are compared with the results obtained by ARGUS [8], CLEO [9] and VENUS [10] in Fig. 3a and to the results obtained by TASSO [5], JADE [6] and TPC/2 γ [7] in Fig. 3b. The quark-diquark model predictions [12] are also shown. Reasonable agreement is found between this measurement and the results obtained by other experiments for $W > 2.3$ GeV. At lower W our measurements agree with the measurements by JADE [6] and ARGUS [8], but lie below the results obtained by CLEO [9], and VENUS [10]. The cross-section measurements reported here extend towards higher values of W than previous results.

Fig. 3a-b show the measured $\gamma\gamma \rightarrow p\bar{p}$ cross-section as a function of W together with some predictions based on the quark-diquark model [11, 12, 15]. There is good agreement between our results and the older quark-diquark model predictions [11, 15]. The most recent calculations [12] lie above the data, but within the estimated theoretical uncertainties the predictions are in agreement with the measurement.

An important consequence of the pure quark hard scattering picture is the power law which follows from the dimensional counting rules [33, 34]. The dimensional counting rules state that an exclusive cross-section at fixed angle has an energy dependence connected with the number of hadronic constituents participating in the process under investigation. We expect that for asymptotically large W and fixed $|\cos\theta^*|$

$$\frac{d\sigma(\gamma\gamma \rightarrow p\bar{p})}{dt} \sim W^{2(2-n)} \quad (7)$$

where $n = 8$ is the number of elementary fields and $t = -W^2/2(1 - |\cos\theta^*|)$. The introduction of diquarks modifies the power law by decreasing n to $n = 6$. This power law is compared to the data in Fig. 3c with $\sigma(\gamma\gamma \rightarrow p\bar{p}) \sim W^{-2(n-3)}$ using three values of the exponent n : fixed values $n = 8$, $n = 6$, and the fitted value $n = 7.5 \pm 0.8$ obtained by taking into account statistical

uncertainties only. More data covering a wider range of W would be required to determine the exponent n more precisely.

The measured differential cross-sections $d\sigma(\gamma\gamma \rightarrow p\bar{p})/d|\cos\theta^*|$ in different W ranges and for $|\cos\theta^*| < 0.6$ are given in Table 4 and in Fig. 4. The differential cross-section in the range $2.15 < W < 2.55$ GeV lies below the results reported by VENUS [10] and CLEO [9] (Fig. 4a). Since the CLEO measurements are given for the lower W range $2.0 < W < 2.5$ GeV, we rescale their results by a factor 0.635 which is the ratio of the two CLEO total cross-section measurements integrated over the W ranges $2.0 < W < 2.5$ GeV and $2.15 < W < 2.55$ GeV. This leads to a better agreement between the two measurements but the OPAL results are still consistently lower. The shapes of the $|\cos\theta^*|$ dependence of all measurements are consistent apart from the highest $|\cos\theta^*|$ bin, where the OPAL measurement is significantly lower than the measurements of the other two experiments.

In Fig. 4b-c the differential cross-sections $d\sigma(\gamma\gamma \rightarrow p\bar{p})/d|\cos\theta^*|$ in the W ranges $2.35 < W < 2.85$ GeV and $2.55 < W < 2.95$ GeV are compared to the measurements by TASSO, VENUS and CLEO in similar W ranges. The measurements are consistent within the uncertainties.

The comparison of the differential cross-section as a function of $|\cos\theta^*|$ for $2.55 < W < 2.95$ GeV with the calculation of [12] at $W = 2.8$ GeV for different distribution amplitudes (DA) is shown in Fig. 5a. The pure quark model [2, 3] and the quark-diquark model predictions lie below the data, but the shapes of the curves are consistent with those of the data.

In Fig. 5b the differential cross-section $d\sigma(\gamma\gamma \rightarrow p\bar{p})/d|\cos\theta^*|$ is shown versus $|\cos\theta^*|$ for $2.15 < W < 2.55$ GeV. The cross-section decreases at large $|\cos\theta^*|$; the shape of the angular distribution is different from that at higher W values. This indicates that for low W the perturbative calculations of [2, 3] are not valid.

Another important consequence of the hard scattering picture is the hadron helicity conservation rule. For each exclusive reaction like $\gamma\gamma \rightarrow p\bar{p}$ the sum of the two initial helicities equals the sum of the two final ones [35]. According to the simplification used in [11], only scalar diquarks are considered, and the (anti) proton carries the helicity of the single (anti) quark. Neglecting quark masses, quark and antiquark and hence proton and antiproton have to be in opposite helicity states. If the (anti) proton is considered as a point-like particle, simple QED rules determine the angular dependence of the unpolarized $\gamma\gamma \rightarrow p\bar{p}$ differential cross-section [29]:

$$\frac{d\sigma(\gamma\gamma \rightarrow p\bar{p})}{d|\cos\theta^*|} \propto \frac{(1 + \cos^2\theta^*)}{(1 - \cos^2\theta^*)}. \quad (8)$$

This expression is compared to the data in two W ranges, $2.55 < W < 2.95$ GeV (Fig. 5a) and $2.15 < W < 2.55$ GeV (Fig. 5b). The normalisation in each case is determined by the best fit to the data. In the higher W range, the prediction (8) is in agreement with the data within the experimental uncertainties. In the lower W range this simple model does not describe the data. At low W soft processes such as meson exchange are expected to introduce other partial waves, so that the approximations leading to (8) become invalid [36].

10 Conclusions

The cross-section for the process $e^+e^- \rightarrow e^+e^-p\bar{p}$ has been measured in the $p\bar{p}$ centre-of-mass energy range of $2.15 < W < 3.95$ GeV using data taken with the OPAL detector at $\sqrt{s_{ee}} = 183$ and 189 GeV. The measurement extends to slightly larger values of W than in previous measurements.

The total cross-section $\sigma(\gamma\gamma \rightarrow p\bar{p})$ as a function of W is obtained from the differential cross-section $d\sigma(e^+e^- \rightarrow e^+e^-p\bar{p})/dW$ using a luminosity function. For the high $p\bar{p}$ centre-of-mass energies, $W > 2.3$ GeV, the measured cross-section is in good agreement with other experimental results [5, 7–10]. At lower W the OPAL measurements lie below the results obtained by CLEO [9], and VENUS [10], but agree with the JADE [6] and ARGUS [8] measurements. The cross-section as a function of W is in agreement with the quark-diquark model predictions of [11, 12].

The power law fit yields an exponent $n = 7.5 \pm 0.8$ where the uncertainty is statistical only. Within this uncertainty, the measurement is not able to distinguish between predictions for the proton to interact as a state of three quasi-free quarks or as a quark-diquark system. These predictions are based on dimensional counting rules [33, 34].

The shape of the differential cross-section $d\sigma(\gamma\gamma \rightarrow p\bar{p})/d|\cos\theta^*|$ agrees with the results of previous experiments in comparable W ranges, apart from in the highest $|\cos\theta^*|$ bin measured in the range $2.15 < W < 2.55$ GeV. In this low W region contributions from soft processes such as meson exchange are expected to complicate the picture by introducing extra partial waves, and the shape of the measured differential cross-section $d\sigma(\gamma\gamma \rightarrow p\bar{p})/d|\cos\theta^*|$ does not agree with the simple model that leads to the helicity conservation rule. In the high W region, $2.55 < W < 2.95$ GeV, the experimental and theoretical differential cross-sections $d\sigma(\gamma\gamma \rightarrow p\bar{p})/d|\cos\theta^*|$ agree, indicating that the data are consistent with the helicity conservation rule.

Acknowledgements

We want to thank Mauro Anselmino, Wolfgang Schweiger, Carola F. Berger, Maria Novella Kienzle-Focacci and Sven Menke for important and fruitful discussions. We particularly wish to thank the SL Division for the efficient operation of the LEP accelerator at all energies and for their close cooperation with our experimental group. In addition to the support staff at our own institutions we are pleased to acknowledge the

Department of Energy, USA,

National Science Foundation, USA,

Particle Physics and Astronomy Research Council, UK,

Natural Sciences and Engineering Research Council, Canada,

Israel Science Foundation, administered by the Israel Academy of Science and Humanities,

Benozio Center for High Energy Physics,

Japanese Ministry of Education, Culture, Sports, Science and Technology (MEXT) and a grant under the MEXT International Science Research Program,

Japanese Society for the Promotion of Science (JSPS),
German Israeli Bi-national Science Foundation (GIF),
Bundesministerium für Bildung und Forschung, Germany,
National Research Council of Canada,
Hungarian Foundation for Scientific Research, OTKA T-029328, and T-038240,
Fund for Scientific Research, Flanders, F.W.O.-Vlaanderen, Belgium.

References

- [1] G.P. Lepage and S.J. Brodsky, Phys. Rev. D22 (1980) 2157.
- [2] G.R. Farrar, E. Maina and F. Neri, Nucl. Phys. B259 (1985) 702.
- [3] D. Millers and J.F. Gunion, Phys. Rev. D34 (1986) 2657.
- [4] V.L. Chernyak and I.R. Zhitnitsky, Nucl. Phys. B246 (1984) 52.
- [5] TASSO Collaboration, M. Althoff et al., Phys. Lett. B130 (1983) 449.
- [6] JADE Collaboration, W. Bartel et al., Phys. Lett. B174 (1986) 350.
- [7] TPC/Two Gamma Collaboration, H. Aihara et al., Phys. Rev. D36 (1987) 3506.
- [8] ARGUS Collaboration, H. Albrecht et al., Z. Phys. C42 (1989) 543.
- [9] CLEO Collaboration, M. Artuso et al., Phys. Rev. D50 (1994) 5484.
- [10] VENUS Collaboration, H. Hamasaki et al., Phys. Lett. B407 (1997) 185.
- [11] M. Anselmino, P. Kroll and B. Pire, Z. Phys. C36 (1987) 89.
- [12] C.F. Berger, B. Lechner and W. Schweiger, Fizika B8 (1999) 371.
- [13] M. Anselmino, F. Caruso, P. Kroll and W. Schweiger, Int. J. Mod. Phys. A4 (1989) 5213.
- [14] P. Kroll, M. Schürmann and W. Schweiger, Int. J. Mod. Phys. A6 (1991) 4107.
- [15] P. Kroll, Th. Pilsner, M. Schürmann and W. Schweiger, Phys. Lett. B316 (1993) 546.
- [16] P. Kroll, M. Schürmann and P.A.M. Guichon, Nucl. Phys. A598 (1996) 435.
- [17] OPAL Collaboration, K. Ahmet et al., Nucl. Instr. Meth. A305 (1991) 275;
M. Hauschild et al., Nucl. Instr. Meth. A314 (1992) 74;
H.M. Fischer et al., Nucl. Instr. Meth. A252 (1986) 331;
R.D. Heuer and A. Wagner, Nucl. Instr. Meth. A265 (1988) 11;
H.M. Fischer et al., Nucl. Instr. Meth. A283 (1989) 492;
M. Arignon et al., Nucl. Instr. Meth. A313 (1992) 103.
- [18] F. Linde, *Charm Production in Two-Photon Collisions*, Ph. D. Thesis, Leiden University (1988).

- [19] J.A.M. Vermaseren, Nucl. Phys. B229 (1983) 347.
- [20] S. Jadach, B.F.L. Ward and Z. Wąs, Comp. Phys. Comm. 79 (1994) 503.
- [21] S. Jadach, B.F.L. Ward and W. Placzek, Phys. Lett. B390 (1997) 298.
- [22] J. Allison et al., Nucl. Instr. Meth. A317 (1992) 47.
- [23] R. Akers et al., Z. Phys. C65 (1995) 47.
- [24] F.E. Low, Phys. Rev. 120 (1960) 582.
- [25] G.A. Schuler, Comp. Phys. Comm. 108 (1998) 279.
- [26] A. Buijs, W.G.J. Langeveld, M.H. Lehto and D.J. Miller, Comp. Phys. Comm. 79 (1994) 523.
- [27] E. Fermi, Z. Phys. 29 (1924) 315;
E.J. Williams, Proc. Roy. Soc. A139 (1933) 163;
C.F. von Weizsäcker, Z. Phys. 88 (1934) 612.
- [28] J.H. Field, Nucl. Phys. B168 (1980) 477.
- [29] V.M. Budnev, I.F. Ginzburg, G.V. Meledin and V.G. Serbo, Phys. Rep. 15 (1974) 181.
- [30] S.J. Brodsky, T. Kinoshita and H. Terazawa, Phys. Rev. D4 (1971) 1532.
- [31] OPAL Collaboration, G. Abbiendi et al., Eur. Phys. J. C21 (2001) 23.
- [32] G.D. Lafferty, T.R. Wyatt, Nucl. Instr. Meth. A355 (1995) 541.
- [33] S.J. Brodsky and G.R. Farrar, Phys. Rev. Lett. 31 (1973) 1153.
- [34] V.A. Matveev, R.M. Muradian and A.N. Tavkhelidze, Nuovo Cim. Lett. 7 (1973) 719.
- [35] S.J. Brodsky and G.P. Lepage, Phys. Rev. D24 (1981) 2848.
- [36] S.J. Brodsky, F.C. Ern e, P.H. Damgaard and P.M. Zerwas, Contribution to ECFA Workshop LEP200, Aachen, Germany, Sep 29 - Oct 1, 1986.

Monte Carlo background process	Number of events generated	Luminosity (fb ⁻¹)	upper limit at 95 % CL
$e^+e^- \rightarrow e^+e^-e^+e^-$ [19]	800 000	1.0	< 0.75
$e^+e^- \rightarrow e^+e^-\mu^+\mu^-$ [19]	600 000	1.0	< 0.75
$e^+e^- \rightarrow e^+e^-\tau^+\tau^-$ [19]	430 000	1.0	< 0.76
$e^+e^- \rightarrow e^+e^-\pi^+\pi^-$ [18]	149 000	0.6	< 1.29
$e^+e^- \rightarrow \tau^+\tau^-$ [20]	80 000	1.0	< 0.74
$e^+e^- \rightarrow \mu^+\mu^-$ [20]	80 000	10.0	< 0.07
$e^+e^- \rightarrow e^+e^-$ [21]	600 000	1.0	< 0.74

Table 1: Number of generated events and corresponding integrated luminosities for the different background processes. Since no events pass the selection cuts, 95% confidence level (CL) upper limits are given for the number of background events expected to contribute to the selected data sample.

trigger class	data (%)	model (%)
(2,1)	56.5 ± 3.9	45.0 ± 2.5
(2,0)	11.2 ± 2.5	16.0 ± 1.7
(1,1)	6.8 ± 2.0	7.3 ± 1.7
(2,2)	25.5 ± 3.4	31.7 ± 2.5

Table 2: Measured and predicted relative frequencies of four different sub-combinations, $(N_{\text{TT}}, N_{\text{TOF}}) = (2,1), (2,0), (1,1)$ and $(2,2)$, which can trigger the $e^+e^- \rightarrow e^+e^-p\bar{p}$ event for events with $W > 2.15$ GeV. The uncertainties are statistical only.

W range (GeV)	$\langle W \rangle$ (GeV)	Events	$d\sigma(e^+e^- \rightarrow e^+e^-p\bar{p})/dW$ (pb/GeV)	$\sigma(\gamma\gamma \rightarrow p\bar{p})$ (nb)
2.15-2.25	2.20	52	5.46 ± 0.76	$2.69 \pm 0.39 \pm 0.28$
2.25-2.35	2.30	33	2.95 ± 0.51	$1.53 \pm 0.27 \pm 0.16$
2.35-2.45	2.40	32	2.53 ± 0.45	$1.39 \pm 0.26 \pm 0.14$
2.45-2.55	2.50	20	1.69 ± 0.38	$0.96 \pm 0.22 \pm 0.10$
2.55-2.75	2.65	18	1.01 ± 0.24	$0.62 \pm 0.22 \pm 0.08$
2.75-2.95	2.85	6	0.28 ± 0.12	$0.19 \pm 0.11 \pm 0.02$
2.95-3.45	3.14	1	0.26 ± 0.26	$0.05^{+0.11}_{-0.04} \pm 0.01$
3.45-3.95	3.64	1	0.28 ± 0.28	$0.05^{+0.11}_{-0.04} \pm 0.01$

Table 3: Number of events and cross-sections for $|\cos\theta^*| < 0.6$. Statistical and systematic uncertainties are also given. A Poisson asymmetric statistical uncertainty, determined within a 68% confidence interval, has been calculated for the last two bins of W with only one selected event.

$ \cos\theta^* $	$2.15 < W < 2.55$ GeV		$2.35 < W < 2.85$ GeV		$2.55 < W < 2.95$ GeV	
	N_{ev}	$\frac{d\sigma(\gamma\gamma \rightarrow p\bar{p})}{d \cos\theta^* }$ (nb)	N_{ev}	$\frac{d\sigma(\gamma\gamma \rightarrow p\bar{p})}{d \cos\theta^* }$ (nb)	N_{ev}	$\frac{d\sigma(\gamma\gamma \rightarrow p\bar{p})}{d \cos\theta^* }$ (nb)
0.00 – 0.10	49	$4.91 \pm 0.70 \pm 0.48$	23	$1.87 \pm 0.39 \pm 0.18$	6	$0.80 \pm 0.33 \pm 0.08$
0.10 – 0.20	43	$4.62 \pm 0.71 \pm 0.45$	23	$1.86 \pm 0.39 \pm 0.19$	4	$0.51 \pm 0.26 \pm 0.05$
0.20 – 0.30	20	$2.61 \pm 0.58 \pm 0.28$	5	$0.50 \pm 0.23 \pm 0.05$	2	$0.23 \pm 0.17 \pm 0.03$
0.30 – 0.40	16	$2.24 \pm 0.56 \pm 0.23$	8	$0.90 \pm 0.32 \pm 0.11$	2	$0.31 \pm 0.22 \pm 0.04$
0.40 – 0.50	6	$1.40 \pm 0.58 \pm 0.19$	8	$1.14 \pm 0.40 \pm 0.14$	6	$1.03 \pm 0.42 \pm 0.13$
0.50 – 0.60	3	$0.67 \pm 0.39 \pm 0.09$	6	$1.28 \pm 0.53 \pm 0.15$	4	$1.17 \pm 0.58 \pm 0.16$

Table 4: Number of data events selected in each bin of $|\cos\theta^*|$ and the measured differential cross-sections $d\sigma(\gamma\gamma \rightarrow p\bar{p})/d|\cos\theta^*|$ for three W ranges. The statistical and systematic uncertainties are also given.

Source of Systematic uncertainties	Systematic uncertainty (%)
Luminosity Function	5.0
Trigger Efficiency	5.0
Monte Carlo statistics ($W < 2.55$ GeV)	4.5
($W > 2.55$ GeV)	6.0
dE/dx cuts ($W < 2.55$ GeV)	0.1
($W > 2.55$ GeV)	5.0
Residual Background	6.0
Total ($W < 2.55$ GeV)	10.3
Total ($W > 2.55$ GeV)	12.1

Table 5: Estimates of relative systematic uncertainties. The total systematic uncertainty is obtained by adding them in quadrature.

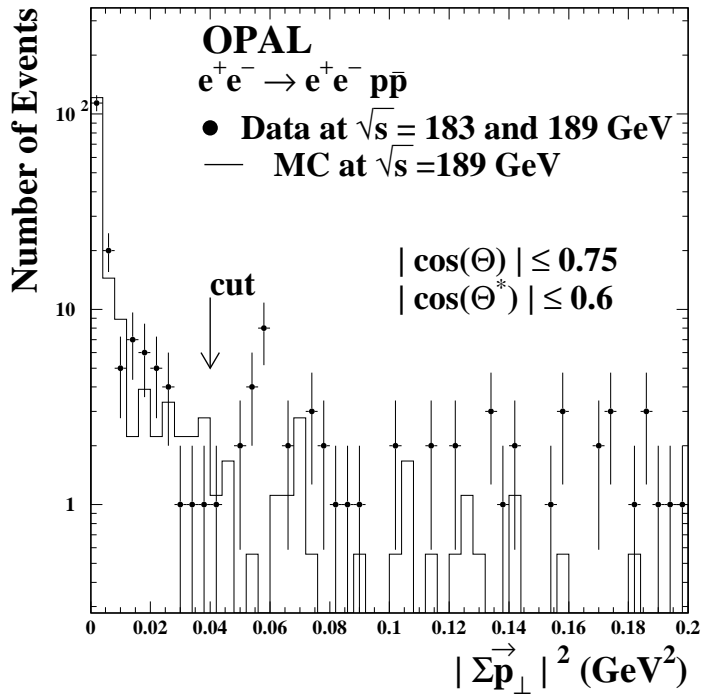


Figure 1: Distribution of the transverse momentum balance, $|\Sigma \vec{p}_\perp|^2$, for the $e^+e^- \rightarrow e^+e^- p\bar{p}$ events in data (black points with error bars) compared to the Monte Carlo simulation (histogram). The distributions are obtained after applying all cuts except the $|\Sigma \vec{p}_\perp|^2$ cut. The arrow indicates the cut value. The error bars are statistical only. The Monte Carlo distribution is normalized to the number of selected data events.

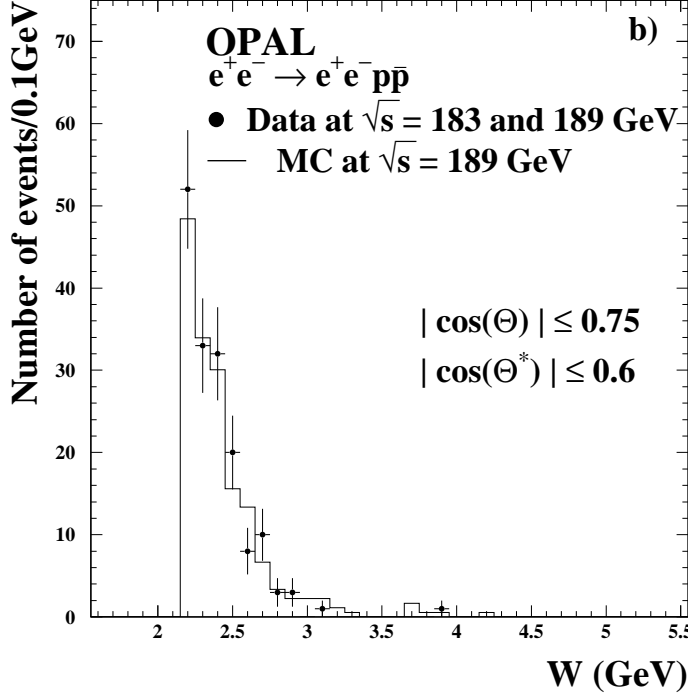
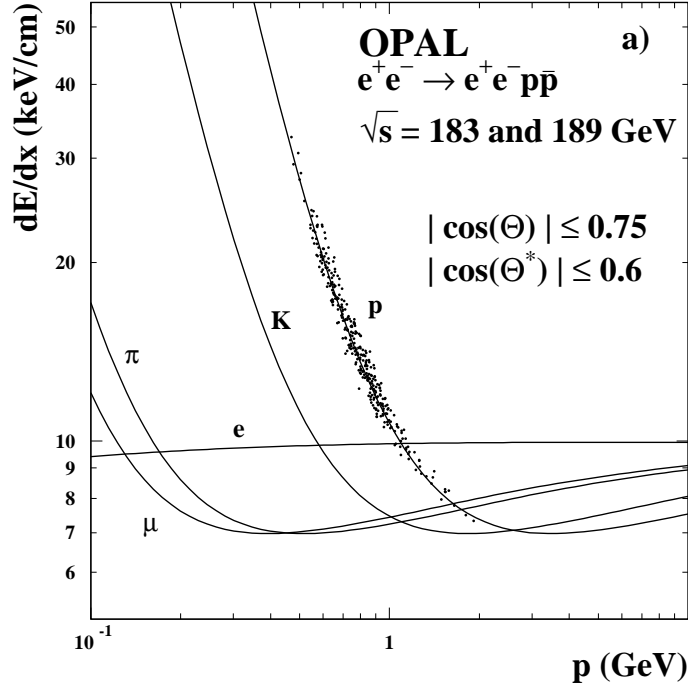


Figure 2: a) Distribution of the specific energy loss, dE/dx , versus the particle momentum p for the proton and antiproton tracks selected by applying the final selection. The curves indicate the expected mean values for different particle species. b) Invariant mass distribution for the 163 selected $e^+e^- \rightarrow e^+e^-p\bar{p}$ events. The dots with error bars are the data, the histogram denotes Monte Carlo events. Errors bars are statistical only. The Monte Carlo distribution is normalized to the number of selected data events.

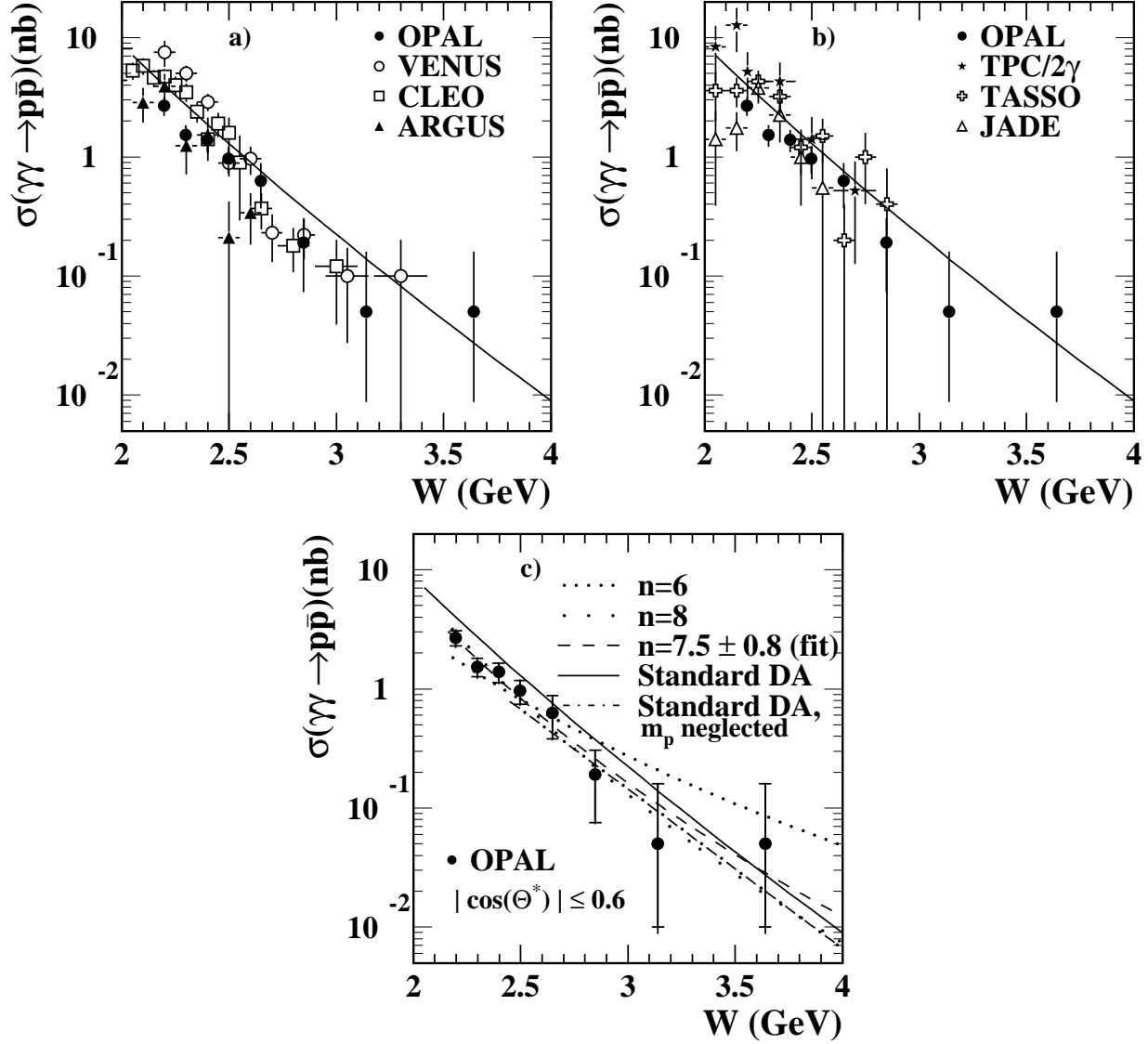


Figure 3: Cross-sections $\sigma(\gamma\gamma \rightarrow p\bar{p})$ as a function of W . The data and the theoretical predictions cover a range of $|\cos\theta^*| < 0.6$. The data points are plotted at the value of $\langle W \rangle$. a,b) The data are compared to other experimental results [7–10] and to the quark-diquark model prediction [12]. The error bars include statistical and systematic uncertainties, except for TASSO [5] where the uncertainties are statistical only. c) The data are compared to the quark-diquark model of [11] (dash-dotted line), and of [12] (solid line), using the standard distribution amplitude (DA) with and without neglecting the mass m_p of the proton, and with the predictions of the power law with fixed and with fitted exponent n . The inner error bars are the statistical uncertainties and the outer error bars are the total uncertainties.

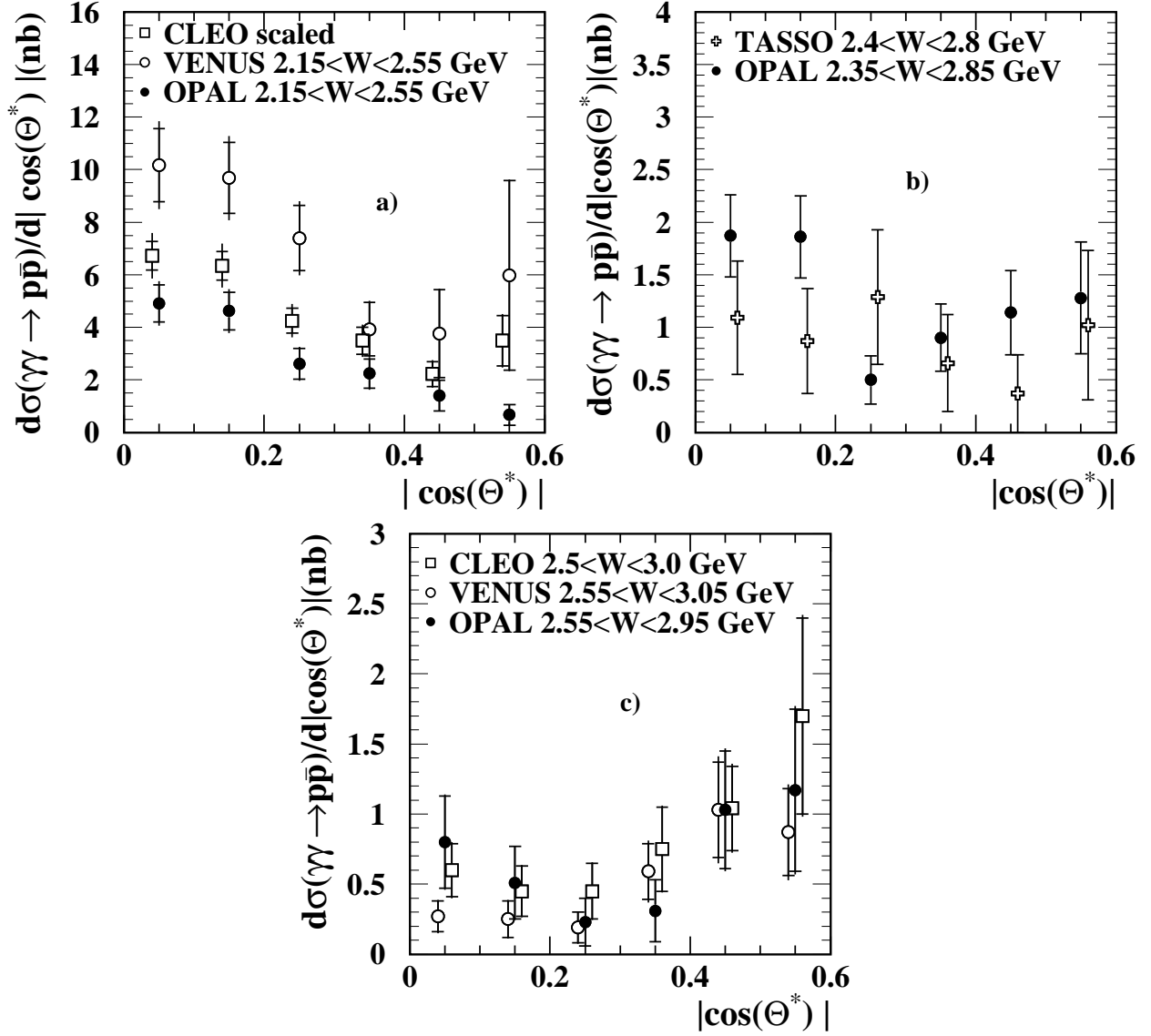


Figure 4: Differential cross-sections for $\gamma\gamma \rightarrow p\bar{p}$ as a function of $|\cos\theta^*|$ in different ranges of W ; a, c) compared with CLEO [9] and VENUS [10] data with statistical (inner error bars) and systematic errors (outer bars), and b) compared with TASSO [5]. The TASSO error bars are statistical only. The data points are slightly displaced for clarity.

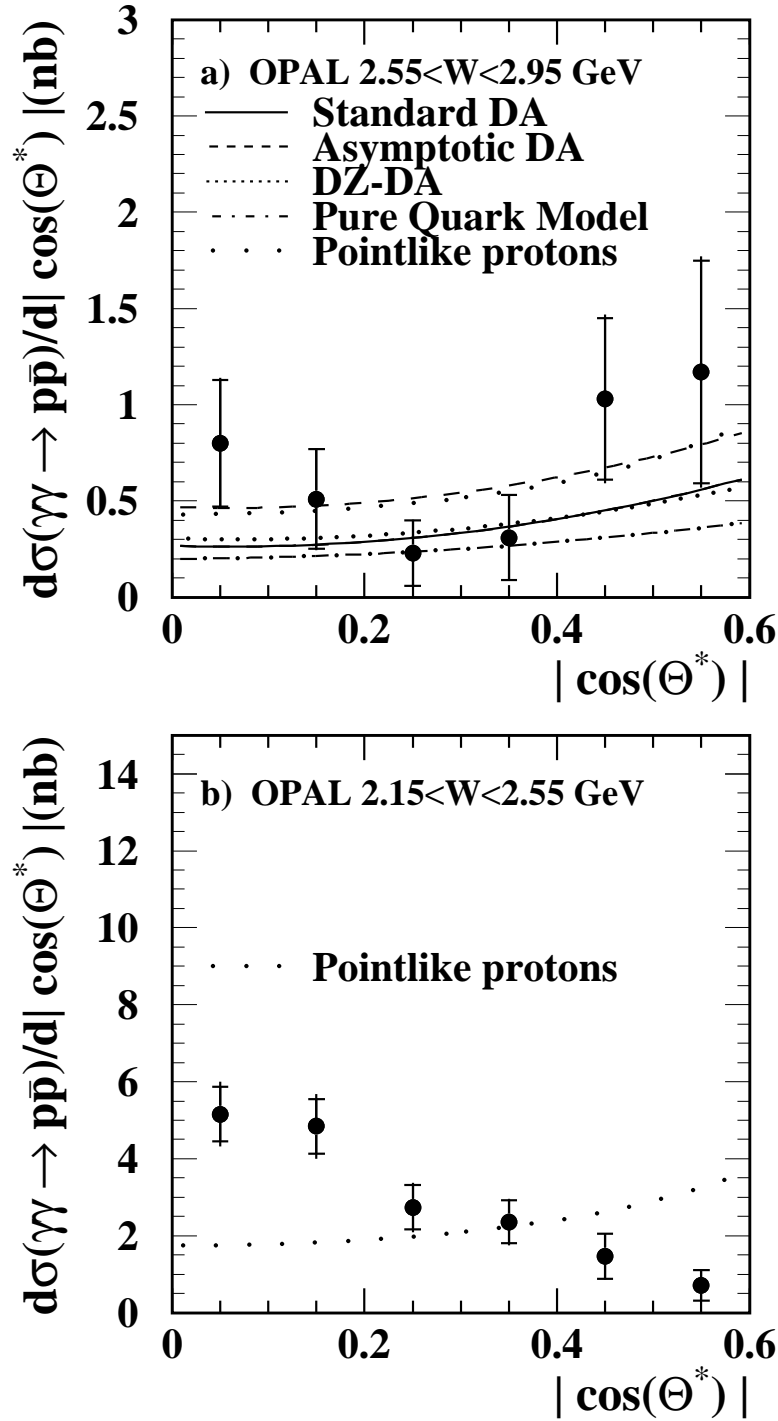


Figure 5: Measured differential cross-section, $d\sigma(\gamma\gamma \rightarrow p\bar{p})/d|\cos\theta^*|$, with statistical (inner bars) and total uncertainties (outer bars) for a) $2.55 < W < 2.95$ GeV and b) $2.15 < W < 2.55$ GeV. The data are compared with the point-like approximation for the proton (8) scaled to fit the data. The other curves show the pure quark model [2], the diquark model of [11] with the Dziembowski distribution amplitudes (DZ-DA), and the diquark model of [12] using standard and asymptotic distribution amplitudes.